Sensors and Actuators: A. Physical 332 (2021) 113125

Contents lists available at ScienceDirect

Sensors and Actuators: A. Physical

journal homepage: www.elsevier.com/locate/sna

Five-axis bimorph monolithic nanopositioning stage: Design, modeling, and characterization

Meysam Omidbeike*, Steven I. Moore, Yuen K. Yong, Andrew J. Fleming[1]

School of Electrical Engineering and Computing, University of Newcastle, Australia

ARTICLE INFO

Article history:
Received 17 February 2021
Received in revised form 1 September 2021
Accepted 16 September 2021
Available online 21 September 2021

Keywords:
Nanopositioning
Atomic force microscopy
Piezoelectric actuators

ABSTRACT

The article describes the design and modeling of a five-axis monolithic nanopositioning stage constructed from a bimorph piezoelectric sheet. Six-axis motion is also possible but requires 16 amplifier channels rather than 8. The nanopositioner is ultra low profile with a thickness of 1 mm. Analytical modeling and finite-element-analysis accurately predict the experimental performance. The stage was conservatively driven with 33% of the maximum voltage, which resulted in an X and Y travel range of 6.22 μm and 5.27 μm respectively; a Z travel range of 26.5 μm; and a rotational motion of 600 μrad and 884 μrad about the X and Y axis respectively. The first resonance frequency occurs at 883 Hz in the Z axis. Experimental atomic force microscopy is performed using the proposed device as a sample scanner.

1. Introduction

The rapid growth in nanotechnology has increased the demand for ultra-precision multi-axis nanopositioning systems [1–3]. In the modern era of nanosystems, many applications require positioning capabilities in more than three degrees-of-freedom (DOF). Multi-axis nanopositioners have enabled a wide range of applications in scanning microscopy [4–7], biotechnology [8], mask/wafer positioning [9,10], nanofabrication [9,11], cell surgery [12] and precision optics [13–16].

Piezoelectric tube scanners were the first three-DOF nanopositioners used in scanning tunneling microscopes [17]. The low cost and simplicity of these monolithic devices have made them popular in applications such as atomic force microscopy [18–20], fiber-optic scanning [21] and endoscopic imaging [22]. However, the tube scanner needs to be long and thin to achieve large displacement. For example, the PT230.94 tube scanner from Physik Instrumente has a length of 30 mm, an outer diameter of 3.2 mm and a thickness of 0.5 mm in order to achieve a travel range of 70 μm. The high-aspect ratio in length and diameter results in low resonance frequencies and high cross-coupling between lateral and vertical axes [23]. To mitigate the above shortfalls, flexure-based nanopositioning systems are used to replace piezoelectric tube scanners in atomic force microscopes [24–27,28,29].

To add rotational positioning capabilities, flexure-based hexapod nanopositioners were introduced [30–33,34]. These devices employ compliant mechanisms composed of metal flexures to create multi-axis linear and rotational displacement. There are a number of drawbacks associated with these devices including relatively large size, complex kinematics, and high cost. A significant advantage of five- and six-axis stages is that they are able to compensate of errors due to cross-coupling. For example, a three axis XYZ stage produces non-zero parasitic rotation that is related to the deflection of the stage. Although it can be minimized by design, high precision applications such as wafer scanning [9] require active compensation requiring six DOF actuation.

To provide a more compact and lower cost alternative to piezoelectric tubes and flexure-based designs, a new class of monolithic nanopositioners constructed from a single piezoelectric sheet was proposed in [1] and [35,36]. In reference [1], a two-DOF monolithic nanopositioner is constructed by removing parts of a piezoelectric sheet to create active flexures that provide guidance and create X and Y axis motion. The device in [1] has an extremely low profile of only 0.5 mm which enables a new range of applications in atomic force microscopy, and particularly, scanning electron microscopy where the load-lock area may be less than 5 mm in height [37]. Sensing and control methods for the two-DOF stage in [1] were reported in [38] and [39].

Compared to other five- and six-axis nanopositioners, which are usually based on the hexapod principle [30–33,34] the proposed device is much smaller, especially in vertical height, but has a lower travel range, lower load capacity and less accuracy. For example, the

* Corresponding author.
E-mail address: meysam.omidbeike@uon.edu.au (M. Omidbeike).
[1] www.precisionmechatronicslab.com

https://doi.org/10.1016/j.sna.2021.113125
0924-4247/

six-axis stage in [34] has a range of 80 μm in the X, Y, Z directions, and 60 μrad of rotation in three axes, with dimensions of 264 mm in diameter and 148 mm in height. The proposed device provides 6 μm deflection in the X and Y axis, 26 μm in the Z axis, and 700 μrad of rotation about the X and Y axis, with dimensions of 63 mm width and 1 mm height, which is less than 1% the height of [34]. The specifications and dimensions of other recently presented six-axis stages are listed in Table IV of [34]. Compared to other work, the proposed device is suited to low-accuracy applications that require a vertical height of less than a few millimeters, a load capacity of less than 10 g, and an X and Y axis deflection of less than 10 μm. Although the proposed design has a much lower stiffness and load capacity than other devices, this permits a much larger rotation about the X and Y axis (about 10× greater than [34]).

1.1. Contribution

This work extends the previous three-axis monolithic nanopositioners to five or six degrees-of-freedom by utilizing a two layer piezoelectric sheet to create active flexures that provide in-plane and out-of-plane motion. This proposed mechanical design utilizes 20 active flexures to develop translation and rotation in, and about, the X, Y and Z axes, respectively. As illustrated in Figs. 1 and 2, each actuator comprises a bimorph piezoelectric beam with a grounded middle layer, and specific voltages applied to the top and bottom electrodes to create in-plane and out-of-plane motion.

A graphical comparison of current and previous designs is shown in Fig. 2, including the unimorph parallel-kinematic design (top), serial kinematic design (middle), and the topic of this work (bottom). Other related work include closed-loop [38] and feedforward control [39] of extension actuators.

A preliminary version of this work was presented at the International Conference on Manipulation, Automation and Robotics at Small Scale (MARSS) [40]. This work used the constitutive piezoelectric equations, and Euler-Bernoulli beam theory to derive a static model for only five degrees-of-freedom due to the limitations of the modeling method. The effective stiffness and mass of the five DOFs were derived to estimate the corresponding resonance frequencies.

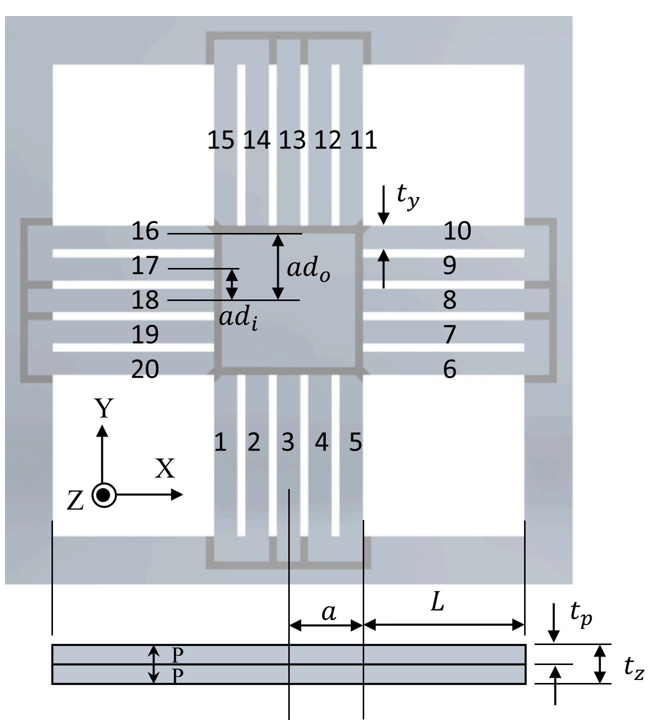

Fig. 1. Dimensions of piezoelectric stage, where d_i and d_o are dimensionless fractions of the half width a.

Compared to [40], the present work uses a combination of constitutive piezoelectric equations, Euler-Bernoulli beam theory, and Hamilton's principle to fully model the statics and dynamics of the nanopositioner in all six DOFs. In addition, the effect of the load on the nanopositioner's first out-of-plane resonance frequency has been modeled. This work also extends on [40] with an experimental identification of modal frequencies and shapes, and includes application to atomic force microscopy imaging.

The remainder of the paper precedes as follows. Section 2 describes the design of the monolithic stage and the actuating principles. Section 3 presents a model of the nanopositioner which is used to derive analytical static rotational and translational gains, resonance frequencies and mode shapes. Finite-element simulations are presented in Section 4, followed by experimental results in Section 5. Section 6 demonstrates the application of the proposed nanopositioner to atomic force microscope imaging.

2. Nanopositioner design and operation

The monolithic nanopositioner is illustrated in Fig. 1. The nanopositioner is fabricated from a bimorph piezoelectric sheet of PZT-5A (PiezoSystems Inc, USA). The bimorph (two-layer) sheet has two external and one internal electrode, which provides the ability to extend and bend. The mechanical and electrode features were created by subtractive ultrasonic machining. The flexures drive a central platform with length $2a$. Each flexure is indexed from 1 to 20 and is of identical length L and width t_y. The thickness of the piezoelectric sheet is t_z. The dimensions d_i and d_o are introduced to parameterize the location at which the flexure is attached to the central platform. Dimensions and material properties of the bimorph nanopositioner are given in Table 1. The stage dimensions were chosen to maximize the X and Y axis travel range, which is achieved by maximizing the flexure length. It is desirable to have a large number of flexures with a minimum of space between each flexure. The thinnest slot that could be cut by ultrasonic machining was 1 mm, which resulted in five flexures per side. The other dimensions are determined by the size of the sheet and central platform, which was 20×20 mm.

The actuating principle for generating six-axis motion is shown in Fig. 3. Knowing that each layer is outwardly poled with the middle layer grounded, the same voltage applied to the top and bottom surface will cause the beam to expand or contract axially and displace the central platform in-plane. When voltages of the opposite sign are applied to the top and bottom surface, the beam bends and displaces the central stage out-of-plane.

To obtain the motion in Fig. 3 a number of independent voltage amplifiers are required. To actuate any single axis, only two amplifier channels are required. To actuate two axes simultaneously (except θ_z), four amplifier channels are required. To actuate the X, Y, and Z axis simultaneously, 8 amplifier channels are required. This configuration can also simultaneously actuate the θ_x and θ_y axes to achieve five-axis motion. However, to obtain a combination of θ_z and any other axis, 16 amplifier channels are required, which is considered to be impractical. Therefore, the proposed design is primarily suited to five-axis motion (and eight amplifier channels). Although rotation around the Z-axis is also possible, this is not experimentally tested in the remainder of the article.

Electrical constraints are applied to the 40 electrodes (20 flexures with two electrodes) to actuate the six DOFs of the nanopositioner. Let $\phi_1^{(i)}$ and $\phi_2^{(i)}$ be the voltages of the top and bottom electrode of the i^{th} flexure. To separate in-plane and out-of-plane motion, the electrode voltages are parameterized in terms of a common mode $\phi_{cm}^{(i)}$ and a differential voltage $\phi_d^{(i)}$ as:

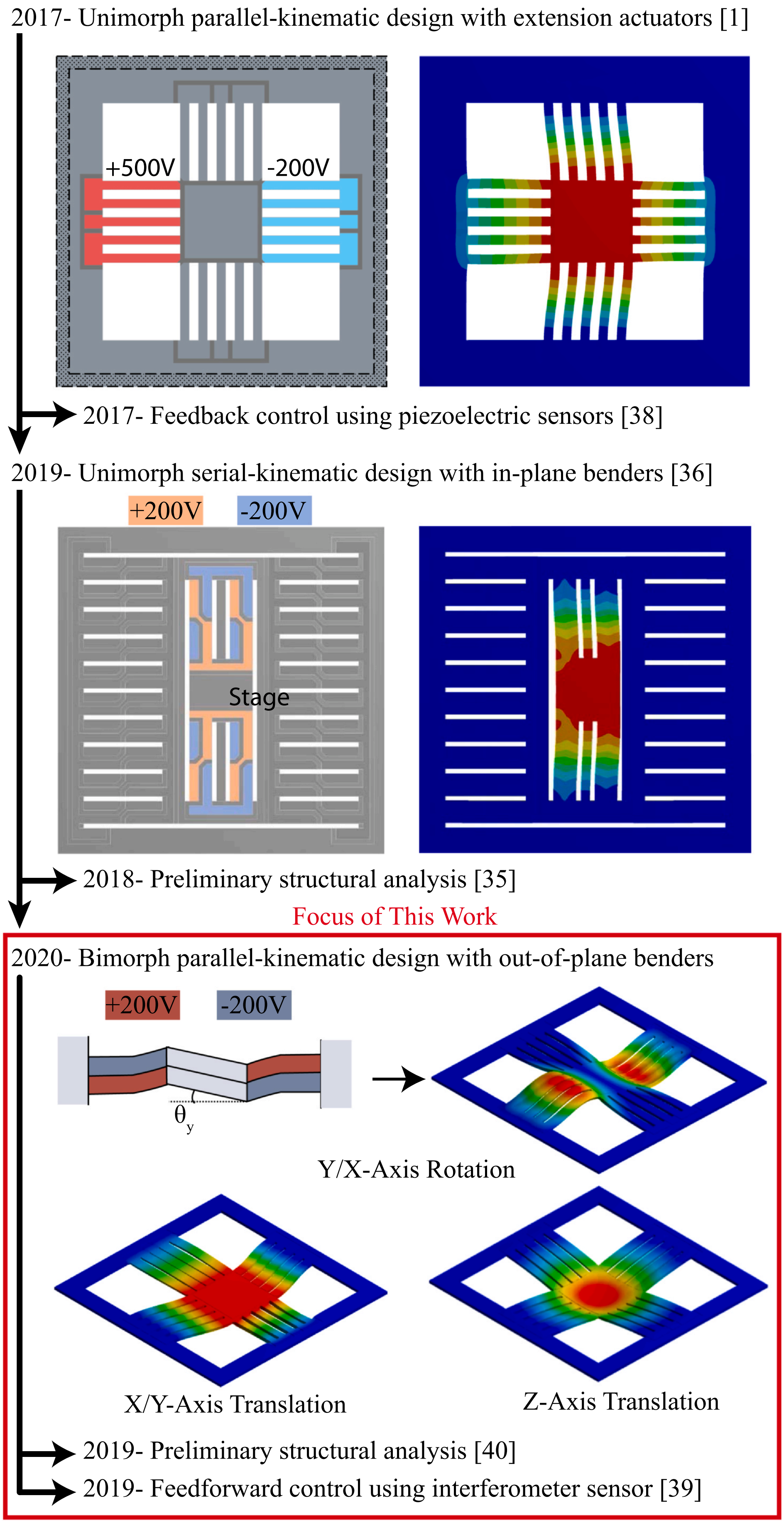
2017- Unimorph parallel-kinematic design with extension actuators [1]
+500V
-200V
2017- Feedback control using piezoelectric sensors [38]
2019- Unimorph serial-kinematic design with in-plane benders [36]
+200V
-200V
Stage
2018- Preliminary structural analysis [35]
Focus of This Work
2020- Bimorph parallel-kinematic design with out-of-plane benders
+200V
-200V
θy
Y/X-Axis Rotation
X/Y-Axis Translation
Z-Axis Translation
2019- Preliminary structural analysis [40]
2019- Feedforward control using interferometer sensor [39]

Fig. 2. The diagram of piezoelectric stage showing the dimension parameters.

Table 1
Dimensions and material properties of the bimorph stage.

Description	Parameter	Value
Thickness of a single piezoelectric layer, mm	t_p	0.5
Thickness of the bimorph sheet, mm	t_z	1.0
Flexure length, mm	L	20.5
Half-length of platform, mm	a	9.5
Width of actuator beam, mm	t_y	3
Poisson's ratio	v	0.35
Young's modulus, GPa	c^E	66
Density, kg/m^3	ρ	7800
Piezoelectric constant, pm/V	d_{31}	-190
Flexure location 1	d_i	0.3889
Flexure location 2	d_o	0.8333

$$\phi_1^{(i)} = \phi_{cm}^{(i)} - \frac{1}{2}\phi_d^{(i)}, \tag{1}$$

$$\phi_2^{(i)} = \phi_{cm}^{(i)} + \frac{1}{2}\phi_d^{(i)}. \tag{2}$$

these voltages are grouped into in-plane and out-of-plane electrical DOFs as:

$$\phi_{ip} = [\phi_{cm}^{(1)}, ..., \phi_{cm}^{(20)}]^T, \tag{3}$$

$$\phi_{op} = [\phi_d^{(1)}, ..., \phi_d^{(20)}]^T. \tag{4}$$

For the six DOFs of the nanopositioner, six control voltages are introduced to parameterize the electrode voltages. They are the control voltages for X axis translation ϕ_{ux}, Y axis translation ϕ_{uy}, Z axis rotation $\phi_{\theta z}$, Z axis translation ϕ_{uz}, X axis rotation $\phi_{\theta x}$, and Y axis rotation $\phi_{\theta y}$. Fig. 3 diagrammatically shows the relationship between the control voltages and the electrode voltages for each DOF of the nanopositioner.

3. Finite DOF nanopositioner model

This section presents the derivation of a 20 degree-of-freedom (DOF) model for the nanopositioner. Firstly, the fundamental principles which govern the dynamics of piezoelectric materials are introduced in Section 3.1. Then, a finite DOF model for each of the piezoelectric flexures and the central stage is derived in Section 3.2 and Section 3.3 respectively. In Section 3.4, the finite DOF models of the individual components are assembled into a single system using kinematic constraints. The final model relates the applied voltages to a set of mechanical DOFs which parameterize the deflection, bending and translation of the stage. In Sections 3.5 and 3.6 the model is used to derive analytical static rotational and translational gains, resonance frequencies and mode shapes.

3.1. Fundamental physical principles

Hamilton's principle is a fundamental variational principle from which the mechanics of a physical system can be derived. This work analyzes the dynamics of a piezoelectric structure in response to external electrical work. For this class of problem Hamilton's principle is expressed as [41–44,45].

$$\delta \int_{t_1}^{t_2} T - H - V \; dt = 0. \tag{5}$$

T is the kinetic energy, H is the enthalpy, V is the potential energy of the externally applied charges, and δ is the variational operator [45]. The energies are formulated as:

$$T = \frac{1}{2}\int_\Omega \rho \dot{u}^T \dot{u} \; dV, \tag{6}$$

$$H = \frac{1}{2}\int_\Omega T^T S - D^T E \; dV, \tag{7}$$

$$V = \int_\Omega q\phi \; dV. \tag{8}$$

The variables are: the displacement field u, the strain field S, the stress field T, the electric field E, the electric displacement D, the charge distribution q, the electric potential ϕ, the material density ρ, and the domain of the structure Ω. The behavior of the piezoelectric material is described by the constitutive equations [44]:

$$T = cS - e^T E, \tag{9}$$

$$D = eS + \varepsilon E, \tag{10}$$

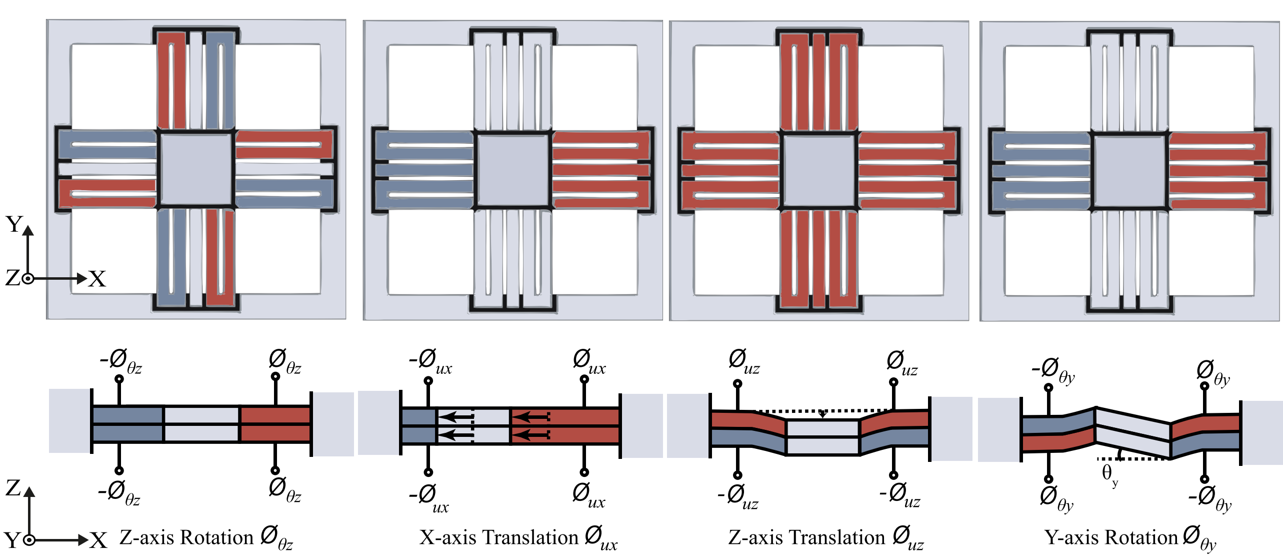

Fig. 3. The actuation scheme for the nanopositioner to control motion in 6 DOFs. A positive applied voltage is shown in red while a negative voltage is shown in blue. The voltages for each actuation mode are also shown, for example $\phi_{\theta y}$ represents the control voltages required to create rotation around the Y axis, and ϕ_{uz} represents the control voltages required to create translation in the Z axis.

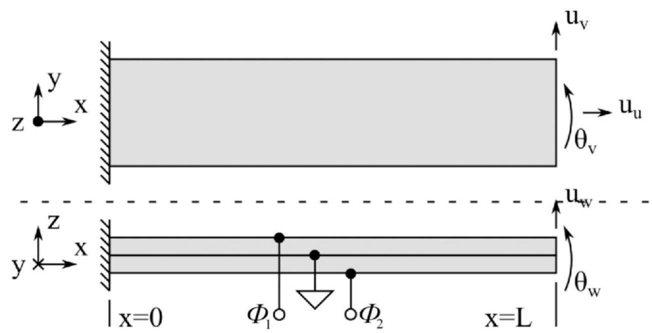

Fig. 4. The five DOF model of the piezoelectric flexure consists of three translational DOFs (u_u, u_v, u_w) and two rotational DOFs (θ_v, θ_w).

where c are the elastic moduli, e are the piezoelectric coefficients, and ε are the dielectric permittivities.

3.2. Piezoelectric flexure dynamics

Using the fundamental principles from Section 3.1, this section outlines the derivation of a 5-DOF model of the piezoelectric flexure shown in Fig. 4. Euler-Bernoulli beam dynamics model the in-plane and out-of-plane deflections of the flexure, and bar dynamics model the extension. Kinematic constraints on the displacement field $u = [u_1, u_2, u_3]^T$ of a flexure are [45]:

$$u_1(x, y, z) = u_0(x) - y\frac{\partial v_0}{\partial x} - z\frac{\partial w_0}{\partial x}, \tag{11}$$

$$u_2(x, y, z) = v_0(x), \tag{12}$$

$$u_3(x, y, z) = w_0(x). \tag{13}$$

Here the displacement field is parameterized in terms of the one-dimensional variables: the out-of-plane deflection w_0, the in-plane deflection v_0, and the axial displacement u_0. There is only one non-zero strain component associated with these kinematics:

$$S_1 = \frac{\partial u_0}{\partial x} - y\frac{\partial 2v_0}{\partial x2} - z\frac{\partial 2w_0}{\partial x2}. \tag{14}$$

The electric field needs to be parameterized in terms of the applied voltages. A parallel plate capacitive structure is assumed. The polarization vector of the two bimorph layers point outward. The electric field has one non-zero component given by:

$$E_3(x, y, z) = \begin{Bmatrix} 2\phi_1/t_z & \text{for} & z \geq 0 \\ 2\phi_2/t_z & \text{for} & z < 0 \end{Bmatrix}, \tag{15}$$

where ϕ_1 and ϕ_2 are the voltages applied to the two electrodes, and t_z is the thickness of the flexure in the Z direction. As per Section 2, the voltages are parameterized in terms of a common mode ϕ_{cm} and a differential voltage ϕ_d:

$$\phi_1 = \phi_{cm} - \frac{1}{2}\phi_d, \tag{16}$$

$$\phi_2 = \phi_{cm} + \frac{1}{2}\phi_d. \tag{17}$$

The charges q_1 and q_2 associated with the voltages ϕ_1 and ϕ_2 are also expressed in terms of a common-mode charge q_{cm} and a differential change q_d:

$$q_1 = q_{cm} - \frac{1}{2}q_d, \tag{18}$$

$$q_2 = q_{cm} + \frac{1}{2}q_d. \tag{19}$$

Since there is only a single non-zero component of both the strain field and the electric field, the constituent equations of the piezoelectric material from (9) and (10) simplify to:

$$T_1 = ES_1 - e_{31}E_3, \tag{20}$$

$$D_3 = e_{31} + \varepsilon_{33}E_3, \tag{21}$$

where E is Young's modulus, e_{31} is the piezoelectric coefficient, and ε_{33} is the dielectric permittivity. Finally, to produce a finite DOF model it is assumed the solutions are a linear combination of trial functions:

$$u_0(x, t) = c_u(t)^T\beta_u(x), \tag{22}$$

$$v_0(x, t) = c_v(t)^T\beta_v(x), \tag{23}$$

$$w_0(x, t) = c_w(t)^T\beta_w(x), \tag{24}$$

where c_u, c_v, and c_w are the DOFs, and b_u, b_v, and b_w are the trial functions for the flexure model, presented in Appendix A. The five selected DOFs are:

$$c_u = u_u, \tag{25}$$

$$c_v = [u_v, \theta_v]^T, \tag{26}$$

$$c_w = [u_w, \theta_w]^T, \tag{27}$$

where u_u, u_v, and u_w are the deflections of the tip of the flexure in axial, in-plane and out-of-plane directions, and θ_v and θ_w is the rotation of the tip in the in-plane and out-of-plane directions. To derive the governing differential equations, (14) to (15) and (20)–(24) are used to evaluate the energy expressions in (6)–(8). Then Hamilton's principle in (5) is evaluated resulting in five differential equations that describe the motion of the piezoelectric flexure:

$$M_{uu}\ddot{c}_u + K_{uu}c_u + K_{u\phi}\phi_{cm} = 0, \tag{28}$$

$$K_{u\phi}^T c_u + K_{\phi\phi}^{cm}\phi_{cm} = -2q_{cm}, \tag{29}$$

$$M_{vv}\ddot{c}_v + K_{vv}c_v = 0, \tag{30}$$

$$M_{ww}\ddot{c}_w + K_{ww}c_w + K_{w\phi}\phi_d = 0, \tag{31}$$

$$K_{w\phi}^T c_u + K_{\phi\phi}^{d}\phi_d = -\frac{1}{2}q_d. \tag{32}$$

The coefficients of the system matrices are presented in Appendix C. Each of the 20 flexures is governed by these differential equations which form part of the full model presented in Section 3.4.

3.3. Plate dynamics

In addition to the flexures, the solid mechanics of the central stage needs to be modeled to accurately account for the dynamics of the nanopositioner. The central stage, shown in Fig. 5 is parameterized as

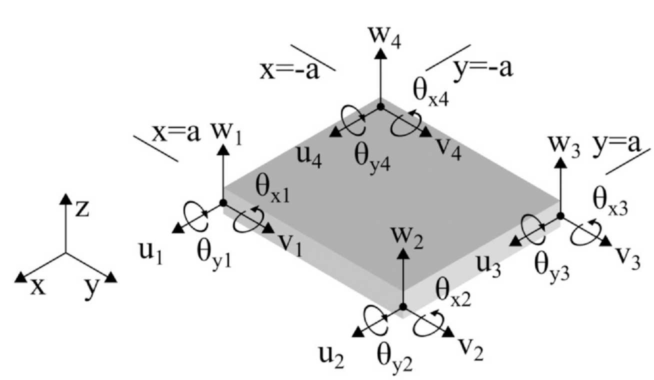

Fig. 5. The model of the square central plate is parameterized by the 20 DOFs which are the translations and rotations in each corner.

a 2D problem utilizing Kirchhoff plate and plane stress kinematics [46]. The kinematic constraints on the displacement field of the plate are:

$$u_1 = \bar{u}_0(x, y, t) - z\frac{\partial \overline{w}_0}{\partial x}, \tag{33}$$

$$u_2 = \bar{v}_0(x, y, t) - z\frac{\partial \overline{w}_0}{\partial y}, \tag{34}$$

$$u_3 = \overline{w}_0(x, y, t). \tag{35}$$

For these kinematics, there are three non-zero strain components:

$$S_1 = \frac{\partial \bar{u}_0}{\partial x} - z\frac{\partial 2\overline{w}_0}{\partial x2}, \tag{36}$$

$$S_2 = \frac{\partial \bar{v}_0}{\partial y} - z\frac{\partial 2\overline{w}_0}{\partial y2}, \tag{37}$$

$$S_6 = \frac{\partial \bar{u}_0}{\partial y} - 2z\frac{\partial 2\overline{w}_0}{\partial 2\partial x}y + \frac{\partial \bar{v}_0}{\partial x}. \tag{38}$$

The material of the plate is considered to be isotropic and despite being formed from a piezoelectric ceramic, the piezoelectric effect is excluded as no voltage is applied to this section of the nanopositioner. Under these conditions, the constitutive equations of the plate are:

$$T = cS, \tag{39}$$

$$\begin{bmatrix} T_1 \\ T_2 \\ T_6 \end{bmatrix} = \begin{bmatrix} c_{11} & c_{12} & 0 \\ c_{12} & c_{11} & 0 \\ 0 & 0 & c_{66} \end{bmatrix} \begin{bmatrix} S_1 \\ S_2 \\ S_6 \end{bmatrix}, \tag{40}$$

where the elastic moduli are a function of Young's Modulus E and Poisson's Ratio ν:

$$c_{11} = \frac{E}{1-\nu^2}, \tag{41}$$

$$c_{12} = \frac{E\nu}{1-\nu^2}, \tag{42}$$

$$c_{66} = \frac{E}{2(1+\nu)}. \tag{43}$$

To form a finite DOF model, solutions for $\bar{u}_0$, $\bar{v}_0$, and $\overline{w}_0$ of the following form are considered:

$$\bar{u}_0(x, y, t) = c_u^T b_u, \tag{44}$$

$$\bar{v}_0(x, y, t) = c_v^T b_v, \tag{45}$$

$$\overline{w}_0(x, y, t) = c_w^T b_w. \tag{46}$$

The trial functions b_u, b_v, and b_w of the plate are presented in Appendix B. The motion of the stage is parameterized by 20 DOFs which are:

$$c_u = [u_1, u_2, u_3, u_4]^T, \tag{47}$$

$$c_v = [v_1, v_2, v_3, v_4]^T, \tag{48}$$

$$c_w = [w_1, \theta_{x1}, \theta_{y1}, \ldots, w_4, \theta_{x4}, \theta_{y4}]^T, \tag{49}$$

where for each corner of the rectangular plate labeled i=1, …, 4, the DOFs u_i, v_i, and w_i are the displacement in the X, Y and Z axes, and the rotations $\theta_x = \frac{\partial \overline{w}_0}{\partial x}$ and $\theta_y = \frac{\partial \overline{w}_0}{\partial y}$.

The displacement/strain fields, constitutive equations, and finite DOF solutions are substituted into the energy expression and Hamilton's principle is evaluated for the following governing equations:

$$B_{uu}\ddot{c}_u + A_{uu}c_u + A_{uv}c_v = 0, \tag{50}$$

$$B_{vv}\ddot{c}_v + A_{uv}^T c_u + A_{vv}c_v = 0, \tag{51}$$

$$B_{ww}\ddot{c}_w + A_{ww}c_w = 0. \tag{52}$$

The coefficients of the system matrices are presented in Appendix D. These equations governing the behavior of the central plate contribute to the system equations presented in Section 3.4.

3.4. The assembled system

The governing equations for the piezoelectric flexures and central stage of the nanopositioner, derived in Section 3.2, are assembled into the system model. There are two independent governing equations for the nanopositioner, one for in-plane motion and one for out-of-plane motion. The two systems are assembled by applying kinematic constraints to the DOFs of the flexures and plate. These constraints are:

$$q_{ip}^{all} = T_{ip}q_{ip}, \tag{53}$$

$$q_{op}^{all} = T_{op}q_{op}. \tag{54}$$

The 100 constraints used to form the matrices T_{ip} and T_{op} are presented in Appendix E. q_{ip}^{all} and q_{op}^{all} includes the DOFs of all the flexures and the plate and q_{ip} and q_{op} are the DOFs of the assembled systems:

$$q_{ip}^{all} = [u_u^{(1)}, \ldots, u_u^{(20)}, u_v^{(1)}, \ldots, u_v^{(20)},]$$
$$\theta_v^{(1)}, \ldots, \theta_v^{(20)}, u_1, \ldots, u_4, v_1, \ldots, v_4]^T, \tag{55}$$

$$q_{ip} = [u_1, \ldots, u_4, v_1, \ldots, v_4]^T. \tag{56}$$

$$q_{op}^{all} = [u_w^{(1)}, \ldots, u_w^{(20)}, \theta_w^{(1)}, \ldots, \theta_w^{(20)},]$$
$$w_1, \theta_{x1}, \theta_{y1}, \ldots, w_4, \theta_{x4}, \theta_{y4}]^T, \tag{57}$$

$$q_{op} = [w_1, \theta_{x1}, \theta_{y1}, \ldots, w_4, \theta_{x4}, \theta_{y4}]^T, \tag{58}$$

The superscript labels the DOFs for each flexure.

Using the mechanical constraints in (53) and (54), the differential equations from (28) to (32) and (50) to (52) for all flexures and the plate are assembled to give the characteristic differential equations of the nanopositioner:

$$M_{ip}\ddot{q}_{ip} + K_{ip}q_{ip} + P_{ip}\phi_{ip} = 0, \tag{59}$$

$$M_{op}\ddot{q}_{op} + K_{op}q_{op} + P_{op}\phi_{op} = 0. \tag{60}$$

Here, K_{ip} and K_{op} are the stiffness matrices, P_{ip} and P_{op} are the piezoelectric matrices, q_{ip} and q_{op} are the mechanical DOFs, M_{ip} and M_{op} are the mass matrices, and ϕ_{ip} and ϕ_{op} are the electrical DOFs for in-plane and out-of-plane.

3.5. Static analysis of the nanopositioner

The trial functions are evaluated to map the eight in-plane DOFs q_{ip} to the X axis translation u_x, Y axis translation u_y, and Z axis rotation θ_z of the center-point:

$$u_x = \frac{1}{4}(u_1 + u_2 + u_3 + u_4), \tag{61}$$

$$u_y = \frac{1}{4}(v_1 + v_2 + v_3 + v_4), \tag{62}$$

$$\theta_z = \frac{1}{8a}(u_1 + u_2 - u_3 - u_4 - v_1 + v_2 + v_3 - v_4). \tag{63}$$

The voltages used to induce in-plane motion of the center point are parameterized by the control voltages ϕ_{ux}, ϕ_{uy}, and $\phi_{\theta z}$ as outlined in Section 2. Equation (59) is solved for the in-plane DOFs for each control voltage. The positioner's X axis translation characteristic equation is:

$$u_x = \frac{2L^3 e_{31} t_y}{5(AEL^2 + 2EI_y)} \phi_{ux}. \tag{64}$$

The mapping from $\phi_{uy} \longrightarrow u_y$ is equivalent to the above expression. The Z axis rotation characteristic equation is:

$$\theta_z = \frac{2L^3 a e_{31} t_y (d_i + d_o)}{AEL^2 a^2 (d_i^2 + d_o^2)} \phi_{\theta z}.$$
$$+ 10EI_y L^2 + 30EI_y(La + a^2) \tag{65}$$

For the out-of-plane system, the trial functions are evaluated to map the twelve out-of-plane DOFs q_{op} to the Z axis translation u_z, X axis rotation θ_x, and Y axis rotation θ_y of the center point:

$$u_z = \frac{1}{4}(w_1 + w_2 + w_3 + w_4) + \frac{1}{8}(\theta_{x1} - \theta_{x2} - \theta_{x3})$$
$$+ \theta_{x4} + \theta_{y1} + \theta_{y2} - \theta_{y3} - \theta_{y4}), \tag{66}$$

$$\theta_x = -\frac{1}{8a}(3w_1 + 3w_2 - 3w_3 - 3w_4 + \theta_{x1} - \theta_{x2})$$
$$+ \theta_{x3} - \theta_{x4} + \theta_{y1} + \theta_{y2} + \theta_{y3} + \theta_{y4}), \tag{67}$$

$$\theta_y = \frac{1}{8a}(3w_1 - 3w_2 - 3w_3 + 3w_4 + \theta_{x1} + \theta_{x2})$$
$$+ \theta_{x3} + \theta_{x4} + \theta_{y1} - \theta_{y2} + \theta_{y3} - \theta_{y4}). \tag{68}$$

The voltages used to induce out-of-plane motion of the center point are parameterized by the control voltages ϕ_{uz}, $\phi_{\theta x}$, and $\phi_{\theta y}$. The out-of-plane DOFs for the above equations are found by solving (60) for each control voltage. The positioner's Z axis translation characteristic equation is:

$$u_z = \frac{15AL^3 e_{31}(2ad_i^2 + 2ad_o^2 + 5L + 5a)}{4(5L^3 c_{11} t_z^3 + 5L^3 c_{12} t_z^3 + 150EI_z L^2)} \phi_{uz}.$$
$$+ 108EI_z a^2 d_i^4 + 108EI_z a^2 d_o^4$$
$$- 144EI_z a^2 d_i^2 d_o^2) \tag{69}$$

For the out-of-plane rotations, after evaluating (60), the terms d_i^4, d_o^4, d_i^6, and d_o^6 are eliminated from the resulting expression as they are considered small due to d_i and d_0 having an absolute value less than one. Therefore the positioner's X axis rotational characteristic equation is:

$$\theta_x = \frac{5AL^3 e_{31}(c_{11} L^3 t_z^3 - 30EI_z a(3L + 2a))}{16EI_z c_{11} L^3 t_z^3 (5L^2 + 15La + 15a^2)} \phi_{\theta x}.$$
$$+ 6a^2(d_i^2 + d_o^2)) + 120E^2 I_z^2 a^2$$
$$(6(d_i^2 + d_o^2)(3L^2 + 3La + a^2) + 5L^2) \tag{70}$$

This expression is equivalent for the mapping from $\phi_{\theta y} \longrightarrow \theta_y$.

3.6. Dynamic analysis of the nanopositioner

The lowest resonance frequencies have the most significant influence on the speed at which the nanopositioner can operate at. The lowest frequencies exist in the out-of-plane direction and modal analysis is performed on the system in (60) to determine both the frequencies and modes shapes, shown in Fig. 6.

The nanopositioner is soft in the out-of-plane direction and the first resonance frequency shifts when a load placed on the stage. By augmenting a fixed mass to the system in (60), the change in resonance frequency can be computed. Fig. 7 plots the change in the first resonance frequency for a load up to 100 g.

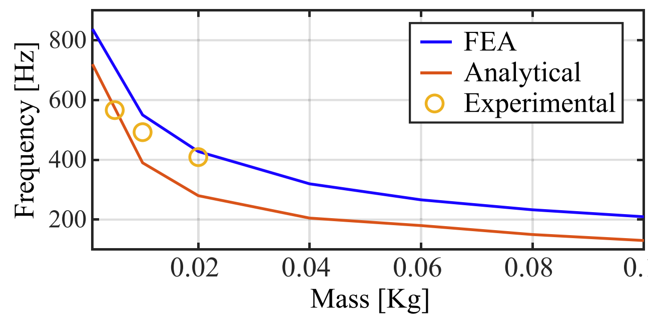

Fig. 7. The analytical, FEA and experimental change in the first resonance frequency with respect to the mass added to the central stage.

4. Finite-element-analysis

A finite-element (FE) model of the stage was constructed using ANSYS workbench. The displacement of all four edges are fixed. The piezoelectric properties of the stage are modeled using the ANSYS Piezo and MEMS Application Customization Toolkit (ACT) extension. The piezoelectric properties for PZT-5A are listed in Table 1. Each piezoelectric layer is polarized outwards along its thickness direction.

To obtain the displacement per unit voltage for $u_{x/y/z}$ and $\theta_{x/y/z}$ along the X, Y and Z axes, +1 V and −1 V are applied to the corresponding electrodes for each DOF as shown in Fig. 3. The respective displacements are obtained. Table 2 compares the simulated and analytical static gains of the stage.

Resonance frequencies of the stage were simulated using the modal analysis module of ANSYS. The first two modes of the monolithic stage are shown in Fig. 8. The first resonance frequency

Table 2
Comparison of the analytical, FE-simulated and experimental results.

	Static gain		
	Analytical	FEA	Exp
X-axis translation (nm/V)	10.35	16.8	15.55
Y-axis translation (nm/V)	10.35	16.8	13.17
Z-axis translation (nm/V)	98.72	50	66.22
X-axis rotation (μrad/V)	1.05	2	1.5
Y-axis rotation (μrad/V)	1.05	2	2.2
Z-axis rotation (μrad/V)	1.6	2.5	-
	Resonance frequency (Hz)		
X/Y-axis translation	20900	21260	-
Z-axis translation	577	883.5	845
X/Y-axis rotation	1220	1960.7	1850

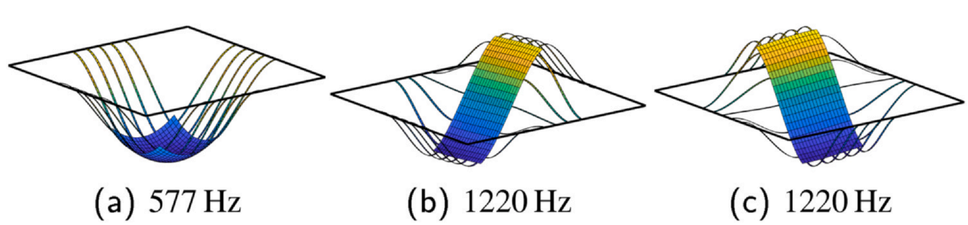

Fig. 6. The first three modes of the nanopositioner exist in the softer out-of-plane direction.

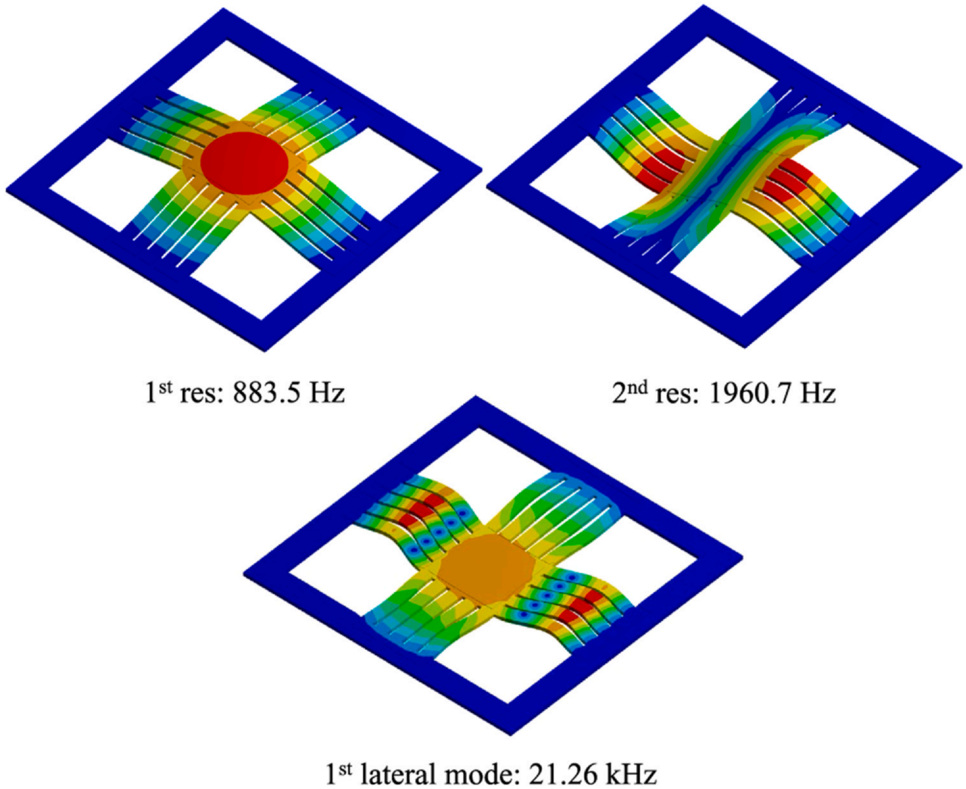

Fig. 8. Finite-element simulated resonance frequencies of the monolithic stage.

appears at 883.5 Hz, translating along the Z axis. The second and third mode is a rotational mode about the X and Y axis, occurs at 1960.7 Hz. To search for the lateral modes along the X and Y axes of the stage, the out-of-plane motions along the Z axis were constrained. The X and Y axis lateral mode occurs at 21.26 kHz. Simulated resonance frequencies are listed in Table 2 together with their analytical counterparts.

5. Experimental results

This section presents the experimental identification and characterization of the sensitivity, range, cross-coupling, and modal responses of the nanopositioner. The experimental setup consists of a nanopositioner mounted on a base as pictured in Fig. 10. The schematic of the experimental set-up is shown in Fig. 9. Here **J** is a transformation matrix that maps the five inputs that relate the translations and rotations to the eight specific electrode voltages. More information on the design of the transformation matrix can be found in [39]. The translational motion in each axis is measured using an MSA-100-3D Laser Doppler Vibrometer (Polytec, Germany). Rotational motions about the X and Y axis are measured using an FPS3010 Interferometer (Attocube, Germany) as pictured in Fig. 10. The sensing configuration allows measurements in five DOFs but rotation around the Z axis.

To evaluate the travel range, electrodes were driven with a 10-Hz sinusoidal voltage from −200 V to +200 V as shown in Fig. 3. The electrodes were driven by an in-house developed 8-channel ± 200 V amplifier. Note that +200 V is only 33% of the full displacement range and was chosen conservatively to ensure a safe operating range for the material. The measured translational motion is 26.5 μm in the Z axis, 6.22 μm in the X axis and 5.27 μm in the Y axis. The rotational motion is 600 μrad and 884 μrad about the X and Y axis respectively. The five-axis motions and their corresponding cross-couplings are measured and plotted in Fig. 13. It can be observed that the cross-coupling from $\theta_X \rightarrow X$ is significant, at about 50% of the X axis travel range. Table 2 compares the analytical, FE-simulated and measured static gains of the monolithic stage. The difference between the predicted and experimental values is primarily due to the uncertainty of the piezoelectric coefficient d_{31} [1]. Other causes of discrepancy include changes in mechanical quality factor, device dimensions and electrical coupling [47].

The hysteresis exhibited by the stage is plotted in Fig. 11. As only 33% of the full range voltage is applied to the system, the maximum hysteresis error measured in the Y axis is about 6%. This is half of the typical PZT-5A hysteresis error which is 14% of the full-scale displacement [48]. In the Z axis, the hysteresis exhibited by the stage is only 2%. The improvement in the hysteresis response is due to the

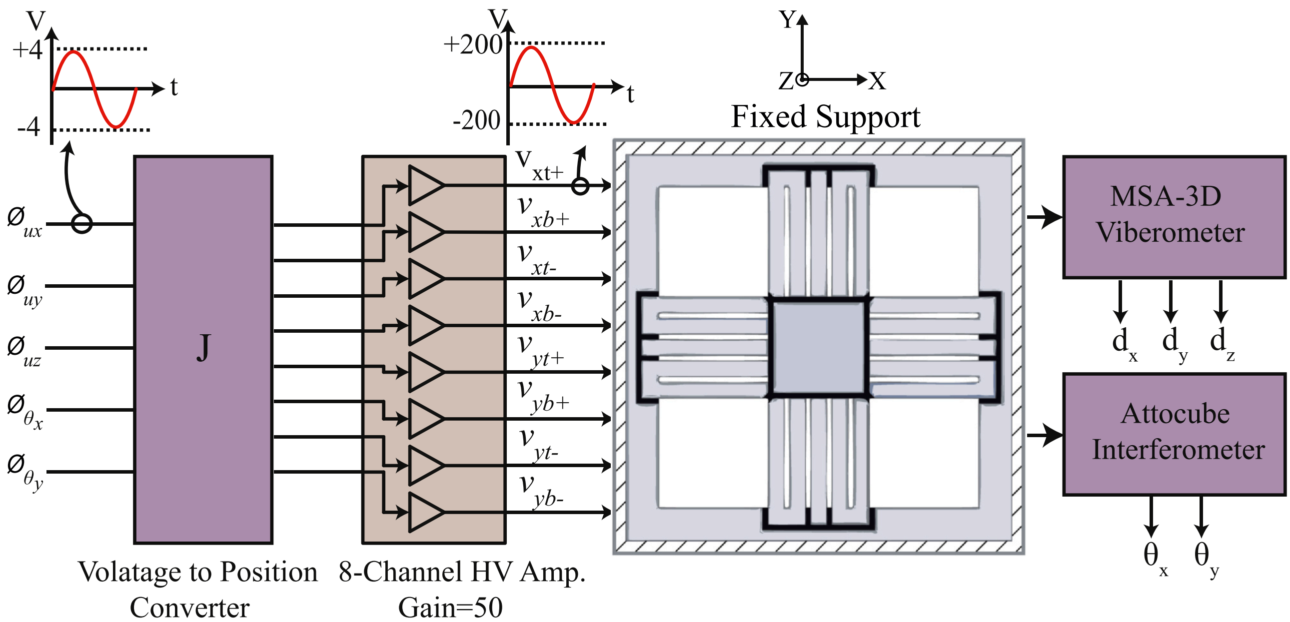

Fig. 9. Experimental configuration of the monolithic nanopositioner. **J** is a transformation matrix generating eight actuation voltages related to the translational and rotational inputs.

push-pull configuration of the top and bottom electrodes which results in partial cancellation of the hysteresis between the two layers. The creep exhibited by the stage in response to a step change in voltage is plotted in Fig. 12. The stage exhibits a creep of 18% after a period of 100 s Fig. 13.

The frequency responses of the nanopositioning stage were measured using the MSA-100 laser vibrometer (Polytec, Germany). A band-limited pseudo random noise input of amplitude 100 mVpk within the frequency range of 100 Hz to 4 kHz was applied to drive each axis. Fig. 15 shows the measured frequency responses of the

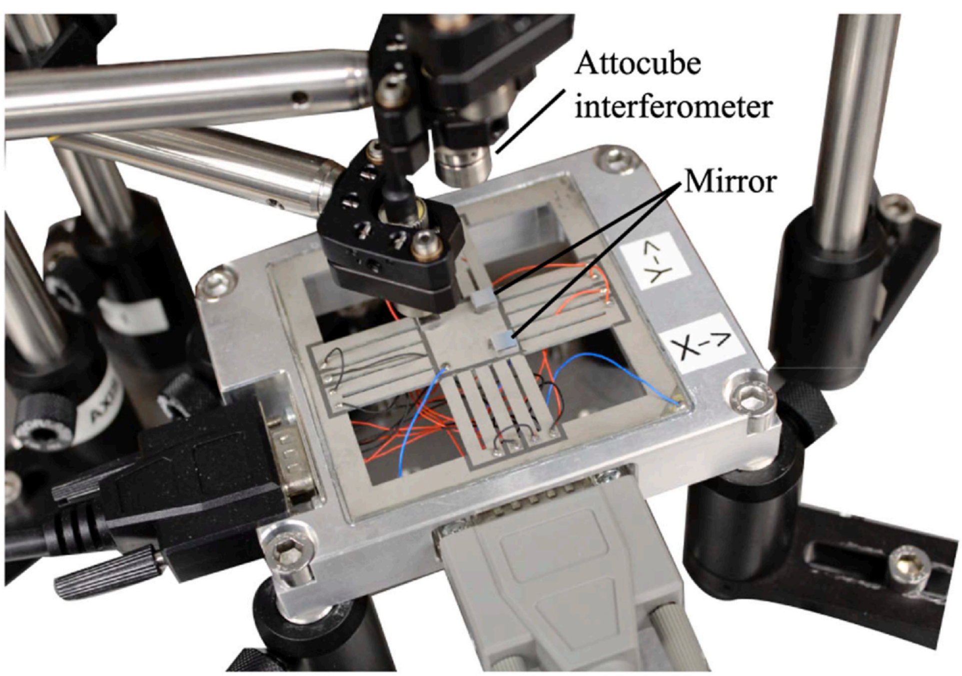

Fig. 10. Monolithic Nanopositioner mounted on a base. Attocube interferometer is used to measure the rotational motions about the X and Y axis.

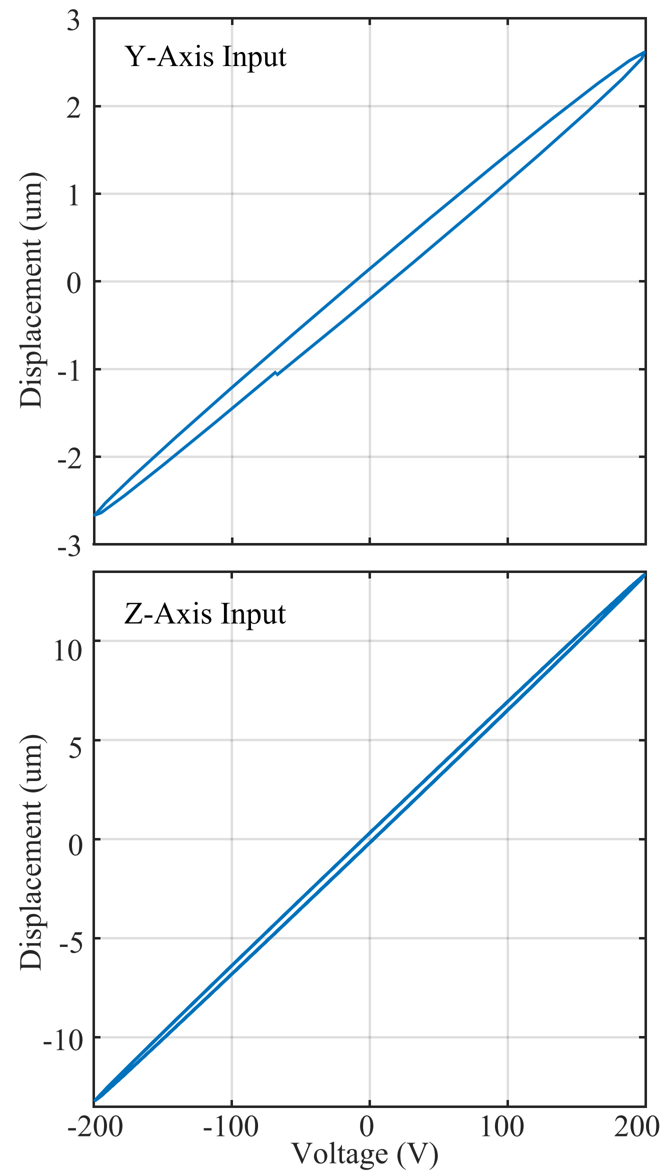

Fig. 11. Hysteresis exhibited by the nanopositioner in the Y and Z axis.

stage. Frequency responses of the translational motion in the X and Y axis exhibit a relatively constant response over a wide frequency range. However, the maximum useful frequency is limited by the first resonance mode in the Z axis occurring at 845 Hz. The measured rotational resonant mode for both θ_x and θ_y appears at 1850 Hz. The

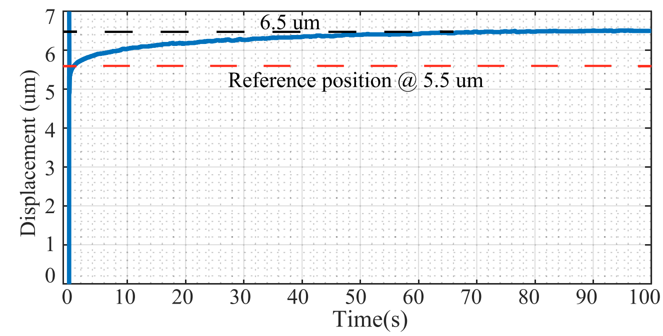

Fig. 12. Creep of actuator motion in open-loop measured over a period of 100 s.

measured resonance frequencies are in close agreement with that of the FE simulations. The effect of the load on the first resonance mode for three masses of 5, 10 and 20 g is experimentally validated. Fig. 7 shows a comparison between the simulated and experimental frequency shift with respect to the mass added to the stage. The two out-of-plane mode shapes observed from the FE results are experimentally validated and shown in Fig. 16. It can be observed that these modes are the dominant resonant peaks limiting the bandwidth of the system in Fig. 15.

The precision of this stage is limited by the amplifier noise voltage which is approximately 1.25 $\mu V/\sqrt{Hz}$. Therefore, the spectral density and standard deviation of the positioning noise can be determined from the frequency responses in Fig. 15 and Eq. (3) in [49]. The noise spectral density in the X and Y axis is 0.013 $pm/\sqrt{Hz}$ or 32 pm (peak-to-peak). Due to the higher sensitivity and lower resonance frequency, the Z-axis noise is significantly higher at 0.12 $pm/\sqrt{Hz}$ or 310 pm (peak-to-peak). These noise figures are similar to piezoelectric tube with the same range.

Since the stage is an open-loop design, the accuracy is limited by hysteresis, which is 6% of the full-scale range in X and Y, and 14% in Z. Therefore, applications requiring high accuracy (< 1% error) would require position sensors and closed-loop control.

6. Atomic force microscope imaging

To demonstrate the application of the proposed monolithic nanopositioner, the experimental setup in Fig. 14 was used to obtain a 5 μm×6 μm image of a Budget Sensors HG-100MG calibration grating. The profile height of the grating is 110 ± 5 nm. The image was obtained using a contact mode cantilever (ContAl-G, Budget-Sensors, Bulgaria) with a resonance frequency of 13 kHz and a nominal stiffness of 0.2 N/m. The grating was imaged in constant-force contact-mode using a Nanosurf Easy Scan 2 at. force microscope (Switzerland) with a 20 nN force setpoint Fig. 15Fig. 16.

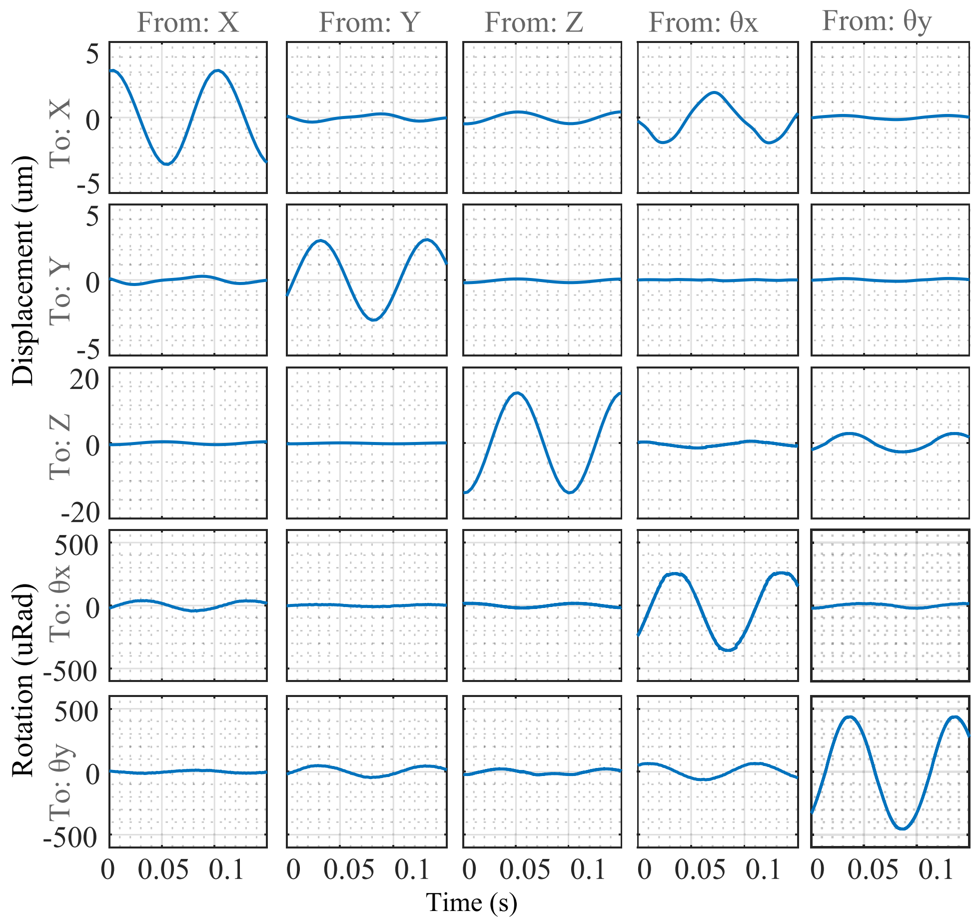

Fig. 13. The measured five-axis motion and cross-coupling in response to a 10-Hz sinusoidal input from −200 V to +200 V applied to each axis.

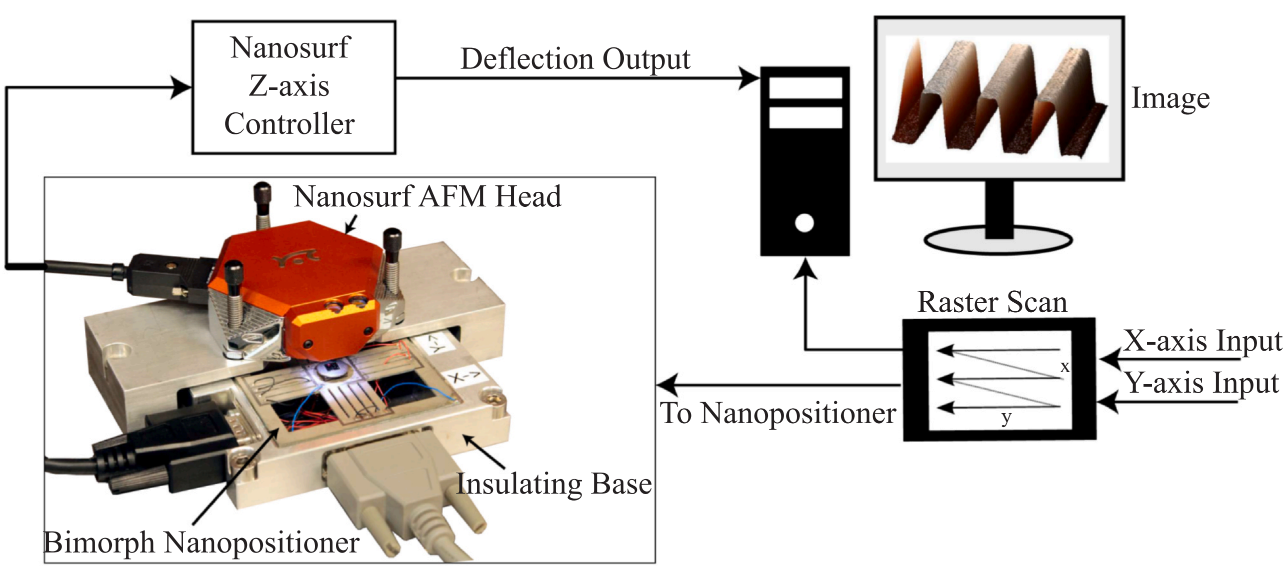

Fig. 14. The schematic of the open-loop AFM imaging using the proposed nanopositioner. The X and Y axis of the nanopositioner are driven in open-loop to create a raster scan. The Z axis controller of the AFM head (Easy Scan 2, Nanosurf, Switzerland) is used to detect the cantilever deflection in the vertical position to create the topography of the sample.

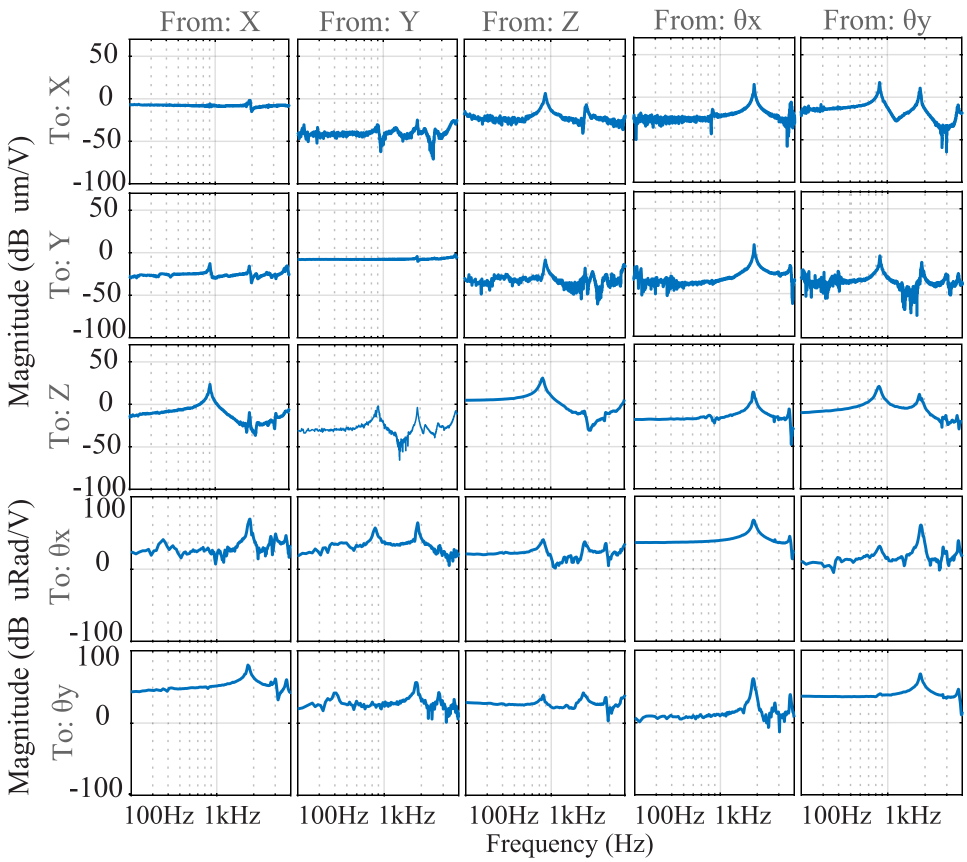

Fig. 15. Measured frequency responses of the monolithic stage.

To move the grating in a raster pattern, the X axis was driven with a 0.5 Hz triangular waveform, and the Y axis was driven with a ramp signal. Note that the nanopositioner was driven in open-loop without any feedforward or feedback control action. The Z axis controller of the Nanosurf AFM was used to detect the cantilever deflection in the vertical position. The deflection output of the AFM was recorded and used to construct the image in Fig. 17. The image processing included the removal of the plane from image, which

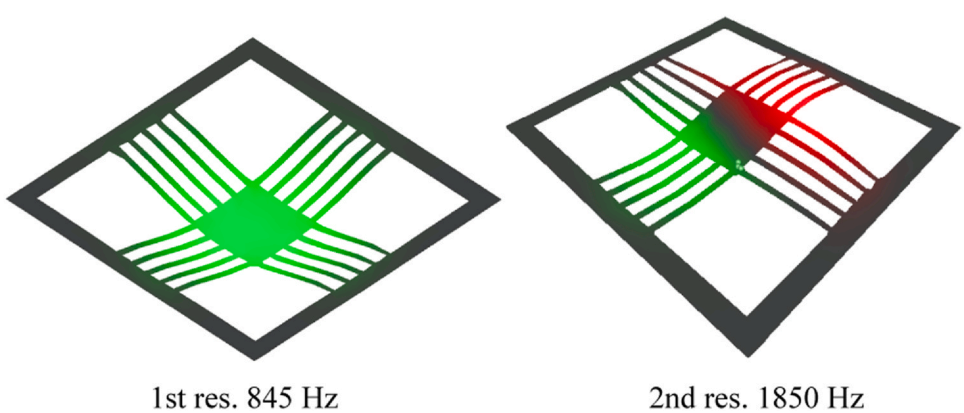

Fig. 16. The measured mode shapes of the nanopositioner using an MSA-100–3D laser vibrometer (Polytec, Germany).

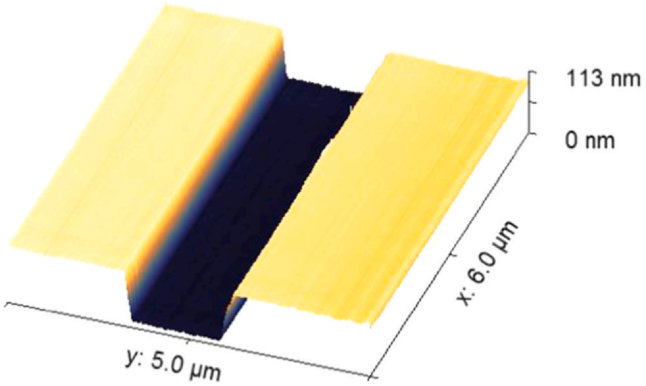

Fig. 17. Constant-force contact-mode AFM image of a calibration grating with a 5 μm pitch and 113 nm height.

results from tilting of the sample and cross-coupling between the lateral and vertical axis. The effect of hysteresis on the image is not observable. This is due to the fact that the scan range is only 33% of the full motion range of the nanopositioner.

7. Conclusions

This paper proposes a new ultra-thin, six-axis monolithic nanopositioner fabricated from a bimorph sheet of piezoelectric material. By driving only 33% of the full-range capacity, the proposed monolithic nanopositioner has a X and Y translational range of 6.2 μm and 5.2 μm respectively, a Z translational range of 26.5 μm, and a rotational range of 600 μrad and 884 μrad about the X and Y axis respectively. The Z resonance frequency appears at 845 Hz, and the rotational resonance mode appears at 1850 Hz. To demonstrate the applications of the proposed stage, an AFM image with 0.5 Hz line rate is obtained. Current research involves the integration of closed-loop sensors and the design of a feedforward controller for cross-coupling compensation. The feedforward design will be combined with a feedback controller to compensate for non-linearity and tracking error.

Declaration of Competing Interest

The authors declare that they have no known competing financial interests or personal relationships that could have appeared to influence the work reported in this paper.

Appendix A. Flexure model: trial functions

The beam is parameterized by five mechanical DOFs. The mechanical DOFs are translations and rotations at the free end of the beam (x=L). They are the axial extension $c_{u,1}$=u_u, the in-plane deflection $c_{v,1}$=u_v, the in-plane rotation $c_{v,2}$=θ_v, the out-of-plane deflection $c_{w,1}$=u_w, and the out-of-plane rotation $c_{w,2}$=θ_w. A fixed boundary condition at the other end of the beam enforces zero translation and rotation at x=0. Trial functions compliant to the continuity requirements of the variational formulation and the boundary conditions at x=0 are [45]:

$$\beta_{u,1}(x) = \frac{x}{L}, \tag{71}$$

$$\beta_{v,1}(x) = \beta_{w,1}(x) = \frac{3x^2}{L^2} - \frac{2x^3}{L^3}, \tag{72}$$

$$\beta_{v,2}(x) = \beta_{w,2}(x) = \frac{x^2}{L} - \frac{x^3}{L^2}. \tag{73}$$

B. Plate model: trial functions

The in-plane motion of the plate is parameterized by eight DOFs. They are the translations of the four corners in the x-direction $c_{u,i}$=u_i, and the translation of the four corners in the y-direction $c_{v,i}$=v_i. The index i refers to each corner: (1) the SW corner, (2) the SE corner, (3) the NE corner, and (4) the NW corner. The trial functions for the in-plane displacements are [46]:

$$b_{u,i}(x, y) = b_{v,i}(x, y) = \frac{1}{4}\left(1 + x_i\frac{x}{a}\right)\left(1 + y_i\frac{y}{b}\right), \tag{74}$$

where b is the length of the plate in the y-direction, a is the length of the plate in the x-direction. In this work a=b. The (x_i, y_i) values associated with each corner are:

$$(x_1, y_1) = (-1, -1), \tag{75}$$

$$(x_2, y_2) = (1, -1), \tag{76}$$

$$(x_3, y_3) = (1, 1), \tag{77}$$

$$(x_4, y_4) = (-1, 1). \tag{78}$$

The out-of-plane motion plate model is parameterized by 12 degrees-of-freedom given by:

$$c_w = [w_1, \theta_{x1}, \theta_{y1}, w_2, \theta_{x2}, \theta_{y2}, w_3, \theta_{x3}, \theta_{y3}, w_4, \theta_{x4}, \theta_{y4}]^T. \tag{79}$$

The degrees of freedom are the deflection w_i at the corners, and rotations at the corners $\theta_{x,i}$, $\theta_{y,i}$. The rotations are defined as:

$$\theta_x = \frac{\partial w_0}{\partial x}, \qquad \theta_y = \frac{\partial w_0}{\partial y}. \tag{80}$$

The trial functions for the plate are [45]:

$$b_{w,i} = \frac{1}{8}\left(1 + x_i\frac{x}{a}\right)\left(1 + y_i\frac{y}{b}\right)\left(2 + x_i\frac{x}{a} + y_i\frac{y}{b} - \frac{x^2}{a^2} - \frac{y^2}{b^2}\right) \tag{81}$$

$$b_{w,i+1} = \frac{1}{8}x_i\left(x_i\frac{x}{a} - 1\right)\left(1 + y_i\frac{y}{b}\right)\left(1 + x_i\frac{x}{a}\right)^2 \tag{82}$$

$$b_{w,i+2} = \frac{1}{8}y_i\left(y_i\frac{y}{b} - 1\right)\left(1 + x_i\frac{x}{a}\right)\left(1 + y_i\frac{y}{b}\right)^2 \tag{83}$$

for each corner i=1, 2, 3, 4.

C. Flexure model: matrix coefficients

Outline here are coefficients of the matrices in the system of equations in (28) to (32). The coefficients of the stiffness matrices in the equations are:

$$K_{uu,ij} = EA\int_0^L \frac{\partial\beta_{u,i}}{\partial x}\frac{\partial\beta_{u,j}}{\partial x}\,dx, \tag{84}$$

$$K_{vv,ij} = EI_y\int_0^L \frac{\partial 2\beta_{v,i}}{\partial x2}\frac{\partial 2\beta_{v,j}}{\partial x2}\,dx, \tag{85}$$

$$K_{ww,ij} = EI_z\int_0^L \frac{\partial 2\beta_{w,i}}{\partial x2}\frac{\partial 2\beta_{w,j}}{\partial x2}\,dx. \tag{86}$$

The coefficients of the piezoelectric matrices are:

$$K_{u\phi,i} = -2t_y e_{31}\int_0^L \frac{\partial\beta_{u,i}}{\partial x}\,dx, \tag{87}$$

$$K_{w\phi,i} = -\frac{1}{4}e_{31}A\int_0^L \frac{\partial 2\beta_{w,i}}{\partial x2}\,dx. \tag{88}$$

The capacitance matrices are comprised of a single element and are given by:

$$K^d_{\phi\phi} = -\frac{\varepsilon_{33}t_y}{t_z}, \tag{89}$$

$$K^{cm}_{\phi\phi} = -\frac{4\varepsilon_{33}t_y}{t_z}. \tag{90}$$

The mass matrix coefficients are:

$$M_{uu,ij} = \rho A\int_0^L \beta_{u,i}\beta_{u,j}\,dx, \tag{91}$$

$$M_{vv,ij} = \rho A\int_0^L \beta_{v,i}\beta_{v,j}\,dx, \tag{92}$$

$$M_{ww,ij} = \rho A\int_0^L \beta_{w,i}\beta_{w,j}\,dx. \tag{93}$$

D. Plate model: matrix coefficients

The coefficients of the stiffness matrices are:

$$A_{uu,ij} = c_{11}t_z\int_A \partial b_{u,i}\partial x\partial b_{u,j}\partial x\,dA + c_{66}t_z\int_A \partial b_{u,i}\partial y\partial b_{u,j}\partial y\,dA \tag{94}$$

$$A_{vv,ij} = c_{11}t_z\int_A \frac{\partial b_{v,i}}{\partial y}\frac{\partial b_{v,j}}{\partial y}\,dA + c_{66}t_z\int_A \frac{\partial b_{v,i}}{\partial x}\frac{\partial b_{v,j}}{\partial x}\,dA \tag{95}$$

$$\begin{aligned} A_{ww,ij} &= c_{11}\frac{t_z^3}{12}\int_A \frac{\partial 2b_{w,i}}{\partial x2}\frac{\partial 2b_{w,j}}{\partial x2}\,dA \\ &+ c_{12}\frac{t_z^3}{12}\int_A \frac{\partial 2b_{w,i}}{\partial y2}\frac{\partial 2b_{w,j}}{\partial x2}\,dA \\ &+ c_{12}\frac{t_z^3}{12}\int_A \frac{\partial 2b_{w,i}}{\partial x2}\frac{\partial 2b_{w,j}}{\partial y2}\,dA \\ &+ c_{11}\frac{t_z^3}{12}\int_A \frac{\partial 2b_{w,i}}{\partial y2}\frac{\partial 2b_{w,j}}{\partial y2}\,dA \\ &+ c_{66}\frac{t_z^3}{12}\int_A \frac{\partial 2b_{w,i}}{\partial x\partial y}\frac{\partial 2b_{w,j}}{\partial x\partial y}\,dA \end{aligned} \tag{97}$$

$$A_{uv,ij} = c_{12}t_z\int_A \frac{\partial b_{u,i}}{\partial x}\frac{\partial b_{v,j}}{\partial y}\,dA + c_{66}t_z\int_A \frac{\partial b_{u,i}}{\partial y}\frac{\partial b_{v,j}}{\partial x}\,dA \tag{98}$$

The coefficients of the mass matrices are:

$$B_{uu,ij} = \rho t_z \int_A b_{u,i} b_{u,j} \, dA, \tag{99}$$

$$B_{vv,ij} = \rho t_z \int_A b_{v,i} b_{v,j} \, dA, \tag{100}$$

$$\begin{aligned} B_{ww,ij} &= \rho t_z \int_A b_{w,i} b_{w,j} \, dA + \frac{\rho t_z^3}{12} \int_A \frac{\partial b_{w,i}}{\partial x} \frac{\partial b_{w,j}}{\partial x} \, dA \\ &\quad + \frac{\rho t_z^3}{12} \int_A \frac{\partial b_{w,i}}{\partial y} \frac{\partial b_{w,j}}{\partial y} \, dA. \end{aligned} \tag{101}$$

The rotary inertia terms (those containing t_z^3) are considered insignificant in this work.

E. Kinematic constraints

Kinematic constraints are used to combine the differential equations for the 20 flexures with those of central plate to produce the governing equations of the system. Constraints exist on the boundary between the flexures and the central plate. First, the following rotations are defined to help define the constraints:

$$\theta_z(x, y) = \frac{1}{2}\left(\frac{\partial \bar{v}_0}{\partial x} - \frac{\partial \bar{u}_0}{\partial y} \right), \tag{102}$$

$$\theta_x(x, y) = \frac{\partial \overline{w}_0}{\partial x}, \tag{103}$$

$$\theta_y(x, y) = \frac{\partial \overline{w}_0}{\partial y}. \tag{104}$$

Each flexure introduces 5 constraint equations which are listed in Table 3 for each flexure referenced by the index i. The terms on the left-hand side of these constraints are the flexure DOFs which are components of the vectors q_{ip}^{all} and q_{op}^{all}, while the right-hand side of these constraints are a function of the plate DOFs which are components of q_{ip} and q_{op}. By evaluating all these constraints the matrix equations in (53) and (54) are formed.

Table 3
The kinematic constraints required to combine the governing equations of the flexures and plate. The right-hand side of these equations are evaluated at (x_i, y_i) which is the point in the plate co-ordinate frame at which the flexure is attached to the central stage.

i=1…5	i=6…10	i=11…15	i=16…20
$u_u^{(i)} = \bar{v}_0$	$u_u^{(i)} = -\bar{u}_0$	$u_u^{(i)} = -\bar{v}_0$	$u_u^{(i)} = \bar{u}_0$
$u_v^{(i)} = -\bar{u}_0$	$u_v^{(i)} = -\bar{v}_0$	$u_v^{(i)} = \bar{u}_0$	$u_v^{(i)} = \bar{v}_0$
$\theta_v^{(i)} = -\theta_z$	$\theta_v^{(i)} = -\theta_z$	$\theta_v^{(i)} = -\theta_z$	$\theta_v^{(i)} = -\theta_z$
$u_w^{(i)} = \overline{w}_0$	$u_w^{(i)} = \overline{w}_0$	$u_w^{(i)} = \overline{w}_0$	$u_w^{(i)} = \overline{w}_0$
$\theta_w^{(i)} = -\theta_y$	$\theta_w^{(i)} = \theta_x$	$\theta_w^{(i)} = \theta_y$	$\theta_w^{(i)} = -\theta_x$

References

[1] A.J. Fleming, Y.K. Yong, An ultrathin monolithic XY nanopositioning stage constructed from a single sheet of piezoelectric material, IEEE/ASME Trans. Mechatron. 22 (6) (2017) 2611–2618.
[2] Y. Yong, S. Aphale, S. Moheimani, Design, identification, and control of a flexure-based XY stage for fast nanoscale positioning, IEEE Trans. Nanotechnol. 8 (1) (2009) 46–54, https://doi.org/10.1109/TNANO.2008.2005829
[3] N. Chen, C. Tian, Design, modeling and testing of a 3-DOF flexible piezoelectric thin sheet nanopositioner, Sens. Actuators A Phys. 323 (2021) 112660, https://doi.org/10.1016/j.sna.2021.112660
[4] M.G. Ruppert, S.I. Moore, M. Zawierta, A.J. Fleming, G. Putrino, Y.K. Yong, Multimodal atomic force microscopy with optimized higher eigenmode sensitivity using on-chip piezoelectric actuation and sensing, Nanotechnology 30 (8) (2019) 085503.
[5] Y.K. Yong, A.J. Fleming, High-speed vertical positioning stage with integrated dual-sensor arrangement, Sens. Actuators A Phys. 248 (2016) 184–192, https://doi.org/10.1016/j.sna.2016.06.042
[6] A. Bazaei, Y.K. Yong, S.R. Moheimani, Combining spiral scanning and internal model control for sequential AFM imaging at video rate, IEEE/ASME Trans. Mechatron. 22 (1) (2016) 371–380.
[7] M. Rana, H. Pota, I. Petersen, Performance of sinusoidal scanning with MPC in AFM imaging, IEEE/ASME Trans. Mechatron. 20 (1) (2015) 73–83.
[8] B.C. Gross, J.L. Erkal, S.Y. Lockwood, C. Chen, D.M. Spence, Evaluation of 3D Printing and its Potential Impact on Biotechnology and the Chemical Sciences (2014).
[9] S. Mishra, J. Coaplen, M. Tomizuka, Precision positioning of wafer scanners segmented iterative learning control for nonrepetitive disturbances [applications of control], IEEE Control Syst. Mag. 27 (4) (2007) 20–25.
[10] H. Lan, Y. Ding, H. Liu, B. Lu, Review of the wafer stage for nanoimprint lithography, Microelectron. Eng. 84 (4) (2007) 684–688.
[11] A. Ferreira, C. Mavroidis, Virtual reality and haptics for nanorobotics, IEEE Robot. Autom. Mag. 13 (3) (2006) 78–92.
[12] Z.-Q. Fan, X.-W. Li, Liu, Piezo-assisted in vitro fertilization of mouse oocytes with spermatozoa retrieved from epididymides stored at 4 degree C, J. Reprod. Dev. (2007) 0801250035-0801250035.
[13] D. Shu, A. Li, S.P. Kearney, C. Mao, J. Anton, R. Harder, X. Shi, T. Mooney, L. Assoufid, Optomechanical design of compact laminar flexure bending mechanism for elliptically bent hard x-ray mirrors, AIP Conf. Proc. 2054 (1) (2019) 060015, https://doi.org/10.1063/1.5084646
[14] D. Shu, S. Kearney, J. Anton, Nanopositioning flexure stages development for synchrotron radiation instrumentation at the advanced photon source, AIP Conf. Proc. 2054 (1) (2019) 060025, https://doi.org/10.1063/1.5084656
[15] G. Genoud, F. Wojda, M. Burza, A. Persson, C.-G. Wahlstrom, Active control of the pointing of a multi-terawatt laser, Rev. Sci. Instrum. 82 (3) (2011), https://doi.org/10.1063/1.3556438 ⟨http://scitation.aip.org/content/aip/journal/rsi/82/3/10.1063/1.3556438⟩.
[16] Y.K. Yong, S.P. Wadikhaye, A.J. Fleming, High speed single- and dual-stage vertical positioners, Rev. Sci. Instrum. 87 (8) (2016) 085104.
[17] G. Binnig, D.P. Smith, Single-tube three-dimensional scanner for scanning tunneling microscopy, Rev. Sci. Instrum. 57 (8) (1986) 1688–1689.
[18] S.O.R. Moheimani, Y.K. Yong, Simultaneous sensing and actuation with a piezoelectric tube scanner (article Number), Rev. Sci. Instrum. 79 (7) (2008) 073702.

[19] Y. Yong, B. Ahmed, S. Moheimani, A 12-electrode piezoelectric tube scanner for fast atomic force microscopy, in: Proceedings of the 2010 American Control Conference, ACC 2010 (2010) 4957–4962 10.1109/ACC.2010.5530941.
[20] D.S. Raghunvanshi, S.I. Moore, A.J. Fleming, Y.K. Yong, Electrode configurations for piezoelectric tube actuators with improved scan range and reduced cross-coupling, IEEE/ASME Trans. Mechatron. 25 (3) (2020) 1479–1486, https://doi.org/10.1109/TMECH.2020.2978241
[21] N. Zhang, T.-H. Tsai, O.O. Ahsen, K. Liang, H.-C. Lee, P. Xue, X. Li, J.G. Fujimoto, Compact piezoelectric transducer fiber scanning probe for optical coherence tomography, Opt. Lett. 39 (2) (2014) 186–188, https://doi.org/10.1364/OL.39.000186 ⟨http://ol.osa.org/abstract.cfm?URI=ol-39-2-186⟩.
[22] S. Vilches, S. Kretschmer, Ç. Ataman, H. Zappe, Miniaturized fourier-plane fiber scanner for OCT endoscopy, J. Micromech. Microeng. 27 (10) (2017) 105015, https://doi.org/10.1088/1361-6439/aa8915 ⟨https://doi.org/10.1088/1361-6439/aa8915⟩.
[23] Y.R. Teo, Y. Yong, A.J. Fleming, A comparison of scanning methods and the vertical control implications for scanning probe microscopy (arXiv), Asian J. Control 20 (4) (2018) 1352–1366, https://doi.org/10.1002/asjc.1422 (arXiv), ⟨https://onlinelibrary.wiley.com/doi/pdf/10.1002/asjc.1422⟩.
[24] Z. Zhang, P. Wang, P. Yan, Y. Guan, A beam flexure-based nanopositioning stage supporting laser direct-write nanofabrication, Sci. China Phys. Mech. Astron. 59 (8) (2016) 684211.
[25] B.J. Kenton, A.J. Fleming, K.K. Leang, Compact ultra-fast vertical nanopositioner for improving scanning probe microscope scan speed, Rev. Sci. Instrum. 82 (12) (2011) 123703.
[26] B.J. Kenton, K.K. Leang, Design and control of a three-axis serial-kinematic high-bandwidth nanopositioner, IEEE/ASME Trans. Mechatron. 17 (2012), pp. 356–368.
[27] Y. Yong, S. Moheimani, B. Kenton, K. Leang, Invited review article: High-speed flexure-guided nanopositioning: mechanical design and control issues, Rev. Sci. Instrum. 83 (12) (2012), https://doi.org/10.1063/1.4765048
[28] See Park Systems, ⟨www.parkafm.com⟩ for information on the use of flexure-based nanopositioning platforms in commercially available AFMs.
[29] See Asylum Research, ⟨http://asylumresearch.com⟩ for information on flexure-based nanopositioning platforms.
[30] H. Shi, H.-J. Su, N. Dagalakis, J.A. Kramar, Kinematic modeling and calibration of a flexure based hexapod nanopositioner, Precis. Eng. 37 (1) (2013) 117–128.
[31] T.-L. Wu, J.-H. Chen, S.-H. Chang, A six-DOF prismatic-spherical-spherical parallel compliant nanopositioner, IEEE Trans. Ultrason. Ferroelectr. Freq. Control 55 (12) (2008) 2544–2551.
[32] M. Ghafarian, B. Shirinzadeh, T.K. Das, A. Al-Jodah, W. Wei, Design of a novel parallel monolithic 6-DOF compliant micromanipulation mechanism, in: Proceedings of the IEEE/ASME International Conference on Advanced Intelligent Mechatronics (AIM), 2018, 997–1002.10.1109/AIM.2018.8452401.
[33] R.M. Panas, M.L. Culpepper, Fabrication of six degrees-of-freedom hexflex positioner with integrated strain sensing using nonlithographically based microfabrication, J. Micro Nano Manuf. 9 (1) (2021) 010902.
[34] D. Zhang, P. Li, J. Zhang, H. Chen, K. Guo, M. Ni, Design and assessment of a 6-DOF micro/nanopositioning system, IEEE/ASME Trans. Mechatron. 24 (5) (2019) 2097–2107, https://doi.org/10.1109/TMECH.2019.2931619
[35] S.I. Moore, M. Omidbeike, A. Fleming, Y.K. Yong, A monolithic serial-kinematic nanopositioner with integrated sensors and actuators, in: Proceedings of the 2018 IEEE/ASME International Conference on Advanced Intelligent Mechatronics (AIM), 2018, 150–155.10.1109/AIM.2018.8452225.
[36] S.I. Moore, Y.K. Yong, M. Omidbeike, A.J. Fleming, Serial-kinematic monolithic nanopositioner with in-plane bender actuators, Mechatronics 75 (102541) (2021), https://doi.org/10.1016/j.mechatronics.2021.102541
[37] C. Zhou, Z. Gong, B.K. Chen, A closed-loop controlled nanomanipulation system for probing nanostructures inside scanning electron microscopes, IEEE/ASME Trans. Mechatron. 21 (3) (2016) 1233–1241, https://doi.org/10.1109/TMECH.2016.2533636
[38] M. Omidbeike, Y.R. Teo, Y.K. Yong, A.J. Fleming, Tracking control of a monolithic piezoelectric nanopositioning stage using an integrated sensor, IFAC-Pap. 50 (1) (2017) 10913–10917.
[39] M. Omidbeike, A.A. Eielsen, Y.K. Yong, A.J. Fleming, Multivariable model-less feedforward control of a monolithic nanopositioning stage with FIR filter inversion, in: Proceedings of the International Conference on Manipulation, Automation and Robotics at Small Scales (MARSS), 2019.
[40] M. Omidbeike, Y.K. Yong, S.I. Moore, A.J. Fleming, A five-axis monolithic nanopositioning stage constructed from a bimorph piezoelectric sheet, in: Proceedings of the 2019 International Conference on Manipulation, Automation and Robotics at Small Scales (MARSS), IEEE, 2019, 1–6.
[41] H. Tiersten, Hamilton's principle for linear piezoelectric media, Proc. IEEE 55 (8) (1967) 1523–1524.
[42] A. Benjeddou, Advances in piezoelectric finite element modeling of adaptive structural elements: a survey, Comput. Struct. 76 (1–3) (2000) 347–363.
[43] L. Meirovitch, Distributed-parameter systems: exact solutions, Fundam. Vib. 1 (2000) 374–458.
[44] V. Piefort, Finite Element Modelling of Piezoelectric Active Structures, Ph.D. thesis, Ph. D. thesis. Bruxelles, Belgium: Université Libre de Bruxelles, Department. (2001).
[45] J.N. Reddy, Energy Principles and Variational Methods in Applied Mechanics, John Wiley & Sons,, 2017.
[46] J.N. Reddy, Mechanics of Laminated Composite Plates and Shells: Theory and Analysis, CRC Press,, 2004.
[47] R. Oria, J. Otero, L. González, L. Botaya, M. Carmona, M. Puig-Vidal, Finite element analysis of electrically excited quartz tuning fork devices, Sensors 13 (6) (2013) 7156–7169.
[48] A.J. Fleming, Quantitative scanning probe microscope topographies by charge linearization of the vertical actuator, Rev. Sci. Instrum. 81 (10) (2010) 103701.
[49] A.J. Fleming, A method for estimating the resolution of nanopositioning systems, Rev. Sci. Instrum. 83 (8) (2012) 086101, https://doi.org/10.1063/1.4739508

Meysam Omidbeike graduated from the University of Newcastle, Australia with a Bachelor of Electrical Engineering in 2015. He is currently a PhD student within the Precision Mechatronics Lab, located in the School of Electrical Engineering and Computer Science, The University of Newcastle. His research focus is on design, sensing and control of monolithic piezoelectric devices including nanopositioning systems, multivariable precision sensing, sensor fusion, and digital signal processing for vibration control.

Steven Ian Moore graduated from the University of Newcastle, Australia with a Bachelor of Electrical Engineering and a Bachelor of Mathematics in 2012, and a PhD degree in electrical engineering in 2016. He is currently a post-doctoral researcher with the Precision Mechatronics Lab at the University of Newcastle. His research focus is on the design, modeling, implementation, and optimization of mechatronic systems including precision motion control and sensing in Microelectromechanical systems (MEMS), structural design of piezoelectric micro-cantilevers, nanopositioning, ultra-high bandwidth fixed point control realizations, image stabilization in optical systems, and inertial stabilization systems.

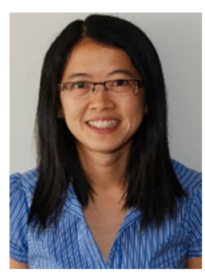

Yuen Kuan Yong received the Bachelor of Engineering degree in Mechatronics Engineering and the PhD degree in mechanical engineering from The University of Adelaide, Australia, in 2001 and 2007, respectively. She was an Australian Research Council DECRA Fellow from 2013 to 2017. She is currently an associate professor with the School of Electrical Engineering and Computing, The University of Newcastle, Australia. Her research interests include nanopositioning systems, design and control of novel micro-cantilevers, atomic force microscopy, and miniature robotics. A/Prof Yong is the recipient of the University of Newcastle Vice-Chancellor's Award for Research Excellence in 2014, and the Vice-Chancellor's Award for Research Supervision Excellence in 2017. She is an associate editor for the IEEE/ASME Transactions of Mechatronics.

Andrew J. Fleming graduated from The University of Newcastle, Australia (Callaghan campus) with a Bachelor of Electrical Engineering in 2000 and Ph.D in 2004. Prof Fleming is the Director of the Precision Mechatronics Lab at The University of Newcastle, Australia. His research interests include lithography, nano-positioning, scanning probe microscopy, and biomedical devices. Prof Fleming's research awards include the ATSE Baterham Medal in 2016, the IEEE Control Systems Society Outstanding Paper Award in 2007, and The University of Newcastle Researcher of the Year Award in 2007. He is the co-author of three books and more than 180 Journal and Conference articles. Prof Fleming is the inventor of several patent applications, and in 2012 he received the Newcastle Innovation Rising Star Award for Excellence in Industrial Engagement.